Journal of Colloid and Interface Science **250,** 422–430 (2002)
doi:10.1006/jcis.2002.8361

Numerical Simulations of Capillary-Driven Flows in Nonuniform Cross-Sectional Capillaries

D. Erickson, D. Li,[1] and C. B. Park

Department of Mechanical & Industrial Engineering, University of Toronto, 5 King's College Road, Toronto, Ontario, Canada M5S 3G8

Received November 5, 2001; accepted March 15, 2002; published online May 15, 2002

In this study the wetting behavior of converging-diverging and diverging-converging capillaries is investigated numerically using an in-house written, finite-element code. An interface tracking procedure based on the predicted change in the total liquid volume, to update the interface location, and Cox's formulation, to determine the dynamic contact angle and the interface shape, is proposed and used. Flow simulations revealed that both converging-diverging and diverging-converging capillaries exhibit significantly slower wetting behavior than straight capillaries and that any deviation in the capillary diameter necessarily tends to slow the overall wetting speed. This behavior was attributed to local regions of very low capillary pressure and high viscous retardation force when the capillary diameter at the interface was significantly larger than the capillary diameter over the upstream fluid. Though the local wetting velocities were different, when equivalent capillaries were compared it was found that both converging-diverging and diverging-converging capillaries had the same total fill time independent of the number of irregular regions, suggesting that the simple model is sufficient for predicting the overall effect. The influence of surface tension and contact angle on the total wetting time was found to be similar for both straight and irregularly shaped capillaries. © 2002 Elsevier Science (USA)

Key Words: **wetting; surface tension; capillary flow; interface tracking.**

1. INTRODUCTION

Studies on the dynamics of capillary wetting can be traced back about 80 years ago to the first basic understanding of the laws of capillarity developed by Lucas (1), Washburn (2), and others (3, 4). While the equations developed in these original studies (or some variant thereof) are still of practical interest (5, 6), many recent studies, for example works on flip chip underfilling (7–9), crystal growth (10), and extrusion processes (11), have examined capillary-driven flows via more general numerical simulations and free surface tracking.

Due to their geometric and analytical simplicity many capillary-driven flow studies have focused on symmetric and uniform cross-sectional geometries. In reality however, most capillaries do not have a constant diameter or cross-section shape. Surface tension-driven wetting phenomena in porous media such as soil, insulation materials, and diapers are significantly influenced by the varying cross section of the capillary. Out of necessity then, a number of works concerned with these and similar phenomena have extended these models to consider irregular geometries. Mason and Morrow (12), for example, reasoned that a triangular cross-sectional geometry had several indicative features of a general pore and developed a model for determining the exact meniscus shape in such a geometry. Turian and Kessler (13) studied 1-D capillary-driven flow in a uniform but noncircular capillary tube. In a later work, Mason and Morrow (14) examined the effects of lengthwise geometric irregularities (including a converging-diverging geometry) on the mean interfacial curvature. Lin and Slattery (15) also considered a converging-diverging geometry as part of their model for two-phase flow through porous media. All of the above studies have focused primarily on determining the interfacial shape and the resulting capillary pressure, rather than modeling the interface progression or dynamic wetting over long distances.

In this study the surface tension-driven, dynamic wetting in converging-diverging and diverging-converging capillary tubes will be examined via finite-element based computational flow simulations. Rather than focusing on the instantaneous interface shape, we examine the fundamental influence of the upstream geometry on the internal flow field and its resulting influence on the dynamic progression of the interface. Difficulties associated with tracking surface tension-driven flows over long distances will be discussed. A simple interface tracking method, based on the change in total liquid volume, is proposed. The proposed method allows for tracking of the interface location over long distances without excessive computation time.

2. NUMERICAL METHOD

Figure 1 is a schematic of two capillaries with varying cross sections along their length, namely a converging-diverging capillary (a), where the entrance and exit regions have a larger diameter than the intermediate region, and a diverging-converging capillary (b), where the entrance and exit regions have a smaller diameter than the intermediate region. The interface location,

[1] To whom correspondence should be addressed. E-mail: dli@mie.utoronto.ca.

0021-9797/02 $35.00

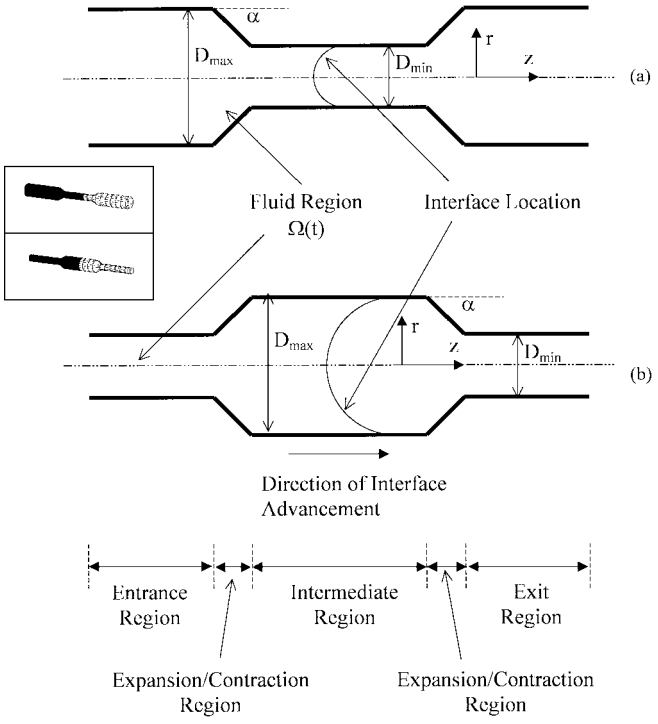

FIG. 1. Capillary tubes with irregular cross sections; (a) converging diverging capillary (b) diverging converging capillary.

marking the boundary between the liquid and the air regions, at a particular time is as illustrated in the figure. For the purposes of this study, we ignore any hydrodynamic effects caused by the air upstream of the interface, as was done by Lowndes (16), and concern ourselves only with the liquid region upstream of the interface, which we define as the computational domain at a particular time, $\Omega(t)$. For an incompressible liquid, the equations governing axis-symmetric flow within this domain are given by

$$\frac{1}{R}\frac{\partial}{\partial R}(RV_r) + \frac{\partial V_z}{\partial Z} = 0, \qquad [1]$$

$$\frac{1}{R}\frac{\partial}{\partial R}(R\tau_{rr}) + \frac{\partial \tau_{zr}}{\partial Z} - \frac{\partial P}{\partial R} + F_r = 0, \qquad [2a]$$

$$\frac{1}{R}\frac{\partial}{\partial R}(R\tau_{rz}) + \frac{\partial \tau_{zz}}{\partial Z} - \frac{\partial P}{\partial Z} + F_z = 0, \qquad [2b]$$

where V_r and V_z are the nondimensional velocity components in the r and z directions, respectively, P is the nondimensional pressure, F_r and F_z represent external body forces applied to the fluid continuum, and R and Z are the nondimensional coordinate directions which have been scaled by the entrance radius r_o ($R = r/r_o$, $Z = z/r_o$). By ignoring the transient and convective terms in the momentum equations, [2a] and [2b], we have limited ourselves to low Reynolds number flows which is consistent with the cases of interest to this study. In the absence of any additional applied body forces, F_r and F_z are replaced by components of the nondimensional gravity force in the r and z directions, respectively. For Newtonian fluids, the relevant components of the stress tensor are given by (again in a nondimensional form)

$$\tau_{rr} = 2\frac{\partial V_r}{\partial R}, \qquad [3a]$$

$$\tau_{zz} = 2\frac{\partial V_z}{\partial Z}, \qquad [3b]$$

$$\tau_{rz} = \frac{\partial V_z}{\partial R} + \frac{\partial V_r}{\partial Z}. \qquad [3c]$$

To account for the Laplace pressure difference at the free interface, we apply a vanishing tangential stress boundary condition and balance the normal stress with the capillary pressure,

$$\tau_{nl} = 0, \qquad [4a]$$

$$\tau_{nn} = \frac{1}{Ca}\left(\frac{1}{R_1} + \frac{1}{R_2}\right), \qquad [4b]$$

where $Ca = \mu v_o/\gamma$ is the capillary number, μ is the viscosity, v_o is a reference velocity, γ is the surface tension, and R_1, R_2 are the local, nondimensional radii of curvature, and the subscripts n and t represent the directions normal and tangential to the interface. A no-slip velocity boundary condition ($V_r = V_z = 0$) is applied at all points along the capillary wall and the appropriate symmetry boundary conditions ($V_r = \partial V_z/\partial R = 0$) are applied at the axis of symmetry shown in Fig. 1. At the capillary inlet we apply a zero gradient boundary condition for the z component of velocity ($\partial V_z/\partial Z = 0$) and a zero radial velocity condition ($V_r = 0$). For most interface tracking methods a slip condition must be applied at or near the solid-liquid-gas three-phase contact line in order to allow the interface to advance with time (7, 16, 17). As will be discussed in Section 2.1, if we are concerned only with the bulk liquid motion the interface tracking approach used here avoids this difficulty.

2.1. Interface Tracking Approach

As alluded to earlier, a number of different free surface tracking methods have been applied to surface tension dominated flows, such as those considered here. In cases where the interface shape and contact line information for steady flows are of primary interest, such as those studied by Lowndes (16) and Tilton (18), rather than the bulk fluid motion (as is the case here), the normal stress iteration has proved successful. Tay *et al.* (7) used a Marker and Boundary method, based on the Marker and Cell technique detailed by Welsh *et al.* (19), for tracking dynamic interfaces in capillary and pressure-driven flows. In their method, surface markers are placed along the interface and then advected forward at each time step using a kinematic condition equivalent to

$$\Gamma(t + \Delta t) = \Gamma(t) + \frac{\partial \Gamma(t)}{\partial t}\Delta t, \qquad [5]$$

where $\Gamma(t)$ is a vector describing the location of a particular surface marker, $\partial\Gamma(t)/\partial t$ is the nodal velocity of the marker as calculated at time t, and Δt is the time step. At each time step the interface shape is reconstructed based on the new location of the surface markers, $\Gamma(t + \Delta t)$, and the new radii of curvature are calculated at each point for use in Eq. [4b]. While very general and applicable to a number of cases, when applied to surface tension-dominated flows the kinematic update schemes like this one require that both the interface location and the shape are determined based on the interfacial velocities at the previous time step. As a result relatively small time steps are required to ensure that the interface shape does not become too distorted. Significant interface distortion can lead to oscillations in the interface velocity, since the flow solution is strongly dependent on the calculated radii of curvature from Eq. [4c]. This limits the ability of these methods to track capillary-driven flows over long distances, with reasonable computational resources.

In this study, a volume displacement approach has been used to avoid this difficulty by tracking only the changes in the system volume and independently determining the interface shape. In general, given the system volume at a particular time, $Q(t)$, the system volume at time $t + \Delta t$ can be estimated by calculating the volume flow rate into the system at time t, $\partial Q(t)/\partial t$, and multiplying by the time step,

$$Q(t + \Delta t) = Q(t) + \frac{\partial Q(t)}{\partial t}\Delta t. \qquad [6]$$

Given $Q(t + \Delta t)$, the new interface location can be determined relatively easily if an approximation to the interface shape can be obtained. While in many cases this may not be possible, for flows in thin capillaries we can assume a spherical interface and approximate hydrodynamic influences on the global interface shape via a dynamic contact angle, θ_d, from Cox's formulation (20),

$$g(\theta_d, \lambda) = g(\theta_e, \lambda) + Ca(t)\ln\left(\varepsilon_s^{-1}\right) + O(Ca), \qquad [7a]$$

$$g(\theta, \lambda) = \int_0^{\theta} \frac{d\beta}{f(\beta, \lambda)}, \qquad [7b]$$

$$f(\beta,\lambda) = \frac{2\sin\beta(\lambda^2(\beta^2 - \sin^2\beta) + 2\lambda(\beta(\pi-\beta) + \sin^2\beta) + ((\pi-\beta)^2 - \sin^2\beta))}{\lambda(\beta^2 - \sin^2\beta)((\pi-\beta) + \sin\beta\cos\beta) + ((\pi-\beta)^2 - \sin^2\beta)(\beta - \sin\beta\cos\beta)}, \qquad [7c]$$

where θ_e is the equilibrium contact angle, λ is the ratio of air and fluid viscosities ($\lambda = \mu_{air}/\mu_{fluid}$), and ε_s is the ratio of the microscopic slip length, s, to a macroscopic characteristic length of the flow system. In Eq. [7a] we calculate an instantaneous capillary number using the interfacial velocity from the previous time step. For the systems considered here an obvious choice for the macroscopic characteristic length is the average channel radius. In previous drop spreading studies (21–23) the microscopic slip length was found to range from approximately 1 to 5 μm. Numerical experiments conducted here revealed that within this range the choice of the microscopic slip length does not significantly affect the overall result; thus for consistency all simulations were conducted with $s = 1$ μm.

While this volume displacement approach is limited to cases where the interface shape can be approximated via some independent formulation, it does have a number of advantages over some of the more complex free surface methods, for the cases of interest here. Since the interface shape and location are being reconstructed based on the system volume, rather than the interface velocities, from the previous time step, much larger time steps can be used resulting in less computationally expensive tracking of capillary flows over long distances. In addition, since the interface velocities are not explicitly required to calculate the volume flux, difficulties with the proper application of a slip condition and the mesh refinement required to capture the proper slip length are avoided (16, 17).

2.2. Comments on Computational Method and Resources

The system of Eqs. [1] through [4b] was solved using the finite element method with isoparameteric, 9-node biquadratic velocity and 4-node bilinear pressure elements (24) using an in-house written code. In all cases a 200-μm initial displacement was taken as the initial system volume (i.e., the initial condition on Eq. [6]). To minimize computational time, a base mesh was formed initially over the entire capillary domain and the elemental matrices were computed for each element. At each time step then the integrations were only carried out over the elements in the region nearest the interface that had been refined to match the interface shape. By this method, the computational time was minimized without losing information on the flow behavior upstream of the interface. Numerical experiments were conducted in order to ensure that the results were independent of both the mesh size and the time step discretization. In general the most efficient scheme was found to be the one in which the time step (from Eq. [6]) was adjusted based on the interfacial velocity, so that at higher interfacial velocities a smaller time step was used and vice versa. For a typical run the real time step varied from as little as 0.001 s at the channel inlet to as high as 1 s near the termination of the computational domain. All simulations were run on a 1000 MHz Pentium III machine with 512 Mbytes of RAM and typically required 2 to 3 h per simulation. For further details on the computational procedure the reader is referred to Appendix A.

3. VERIFICATION OF NUMERICAL METHOD: RISING OF A LIQUID IN A CAPILLARY

In order to verify the interface tracking technique and the numerical code, the rising of a liquid subject to gravity in a capillary of uniform cross section will be used as a test problem. In the limit of low Reynolds number, this capillary rising problem is described by the Lucas-Washburn equation (6),

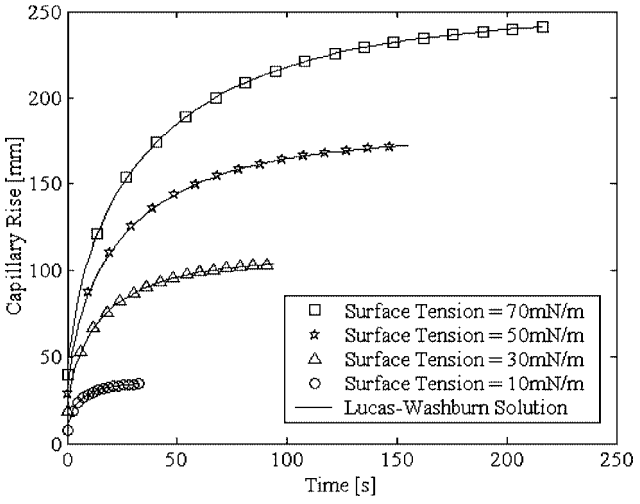

FIG. 2. Comparison of numerical prediction with analytical solution for dynamic capillary rise in a 100-μm-diameter capillary tube with $\theta_e = 30^\circ$, $\rho = 1000$ kg/m^3, and $\mu = 0.001$ kg/ms.

$$h\frac{dh}{dt} + \frac{\rho g D^2}{32\mu}h - \frac{\gamma \cos\theta_e D}{8\mu} = 0, \qquad [8]$$

where h is the height of the capillary rise, D is the capillary diameter, ρ is the liquid density, and g is gravity. For a detailed discussion regarding the applicability and solution methods for this equation, the reader is referred to Zhmud *et al*. (6).

Figure 2 compares the solution to Eq. [8] with that predicted from the numerical model described above (for graphical clarity some simulation data points have been omitted) in a 100-μm-diameter capillary for a number of different surface tension values ranging from 10 to 70 mN/m with $\theta_e = 30^\circ$, $\rho = 1000$ kg/m^3, and $\mu = 0.001$ kg/ms. Simulations were terminated when the relative change in the height of capillary rise over the course of one time step was less than 0.01%. As can be seen in all cases the numerical predictions are essentially identical to the solutions of Eq. [8], thereby suggesting that both the numerical code and the interface tracking procedure are valid. In some cases, a slight lagging, not visible in Fig. 2, of the simulation result behind the solution to Eq. [8] was observed. This was attributed to the constant contact angle assumption implied by Eq. [8]. The introduction of a dynamic advancing contact angle, which is larger than θ_e for an advancing interface, tends to increase the interfacial radii of curvature, thereby reducing the value of the capillary pressure, Eq. [4b], and resulting in slower progression of the interface.

4. DYNAMIC WETTING IN CONVERGING-DIVERGING AND DIVERGING-CONVERGING CAPILLARIES

The main purpose of this study is to investigate dynamic wetting in capillaries with irregular cross sections. Specifically this study will focus on converging-diverging and diverging-converging capillaries as illustrated in Fig. 1.

4.1. Influence of the Varying Cross Section of Capillary

To compare the two geometries, simulations were conducted for a converging-diverging capillary and a diverging-converging capillary, each with $D_{max} = 100$ μm and $D_{min} = 50$ μm (see Fig. 1). The total length of the entrance and exit stages is 20 mm each and the middle stage has a length of 40 mm (not including the contraction and expansion regions) so that average capillary diameter over the length of the simulation domain is 75 μm. In each case the simulation parameters are $\gamma = 30$ mN/m, $\theta_e = 30^\circ$, $\rho = 1000$ kg/m^3, and $\mu = 0.001$ kg/ms; the angle α, as shown in Fig. 1, was fixed at 0.5°. Figure 3 shows the flow field and resulting streamlines for both cases at an arbitrary time t, when the free interface is in the exit region but prior to reaching the end of the simulation domain.

In Fig. 4, the interface position with time for the above simulations is compared with results obtained for two straight capillaries with diameters of 50 and 100 μm, respectively. Most obvious in this figure is that in both cases the capillaries with varying cross sections reach the termination point significantly later than the straight capillaries. In both cases, this can be attributed to a region of extremely slow progression in the large

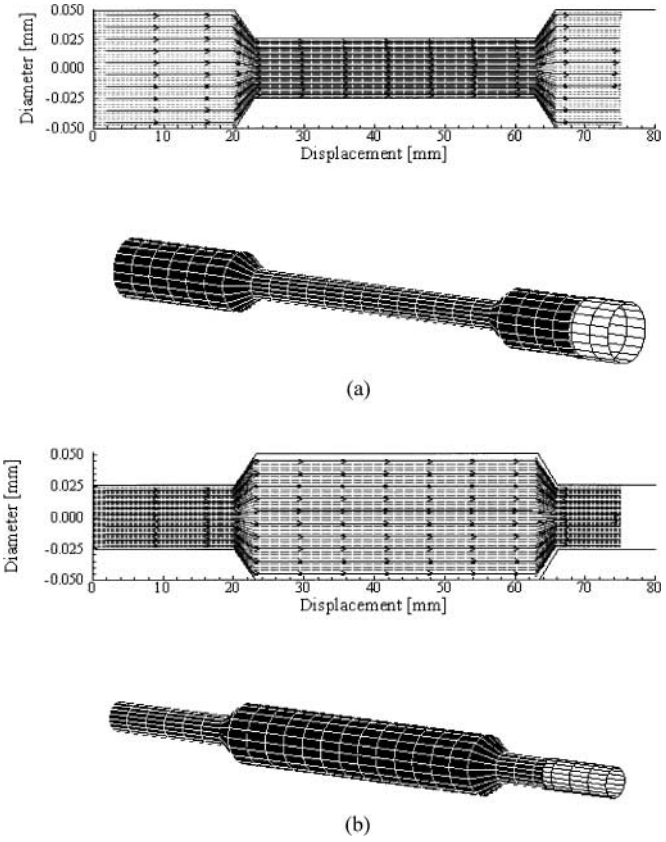

FIG. 3. Streamlines for capillary-driven flow through (a) a converging diverging capillary and (b) a diverging-converging capillary. Darkened region in the lower 3D images represent the wetted surface. In the upper image streamlines terminate at free interface.

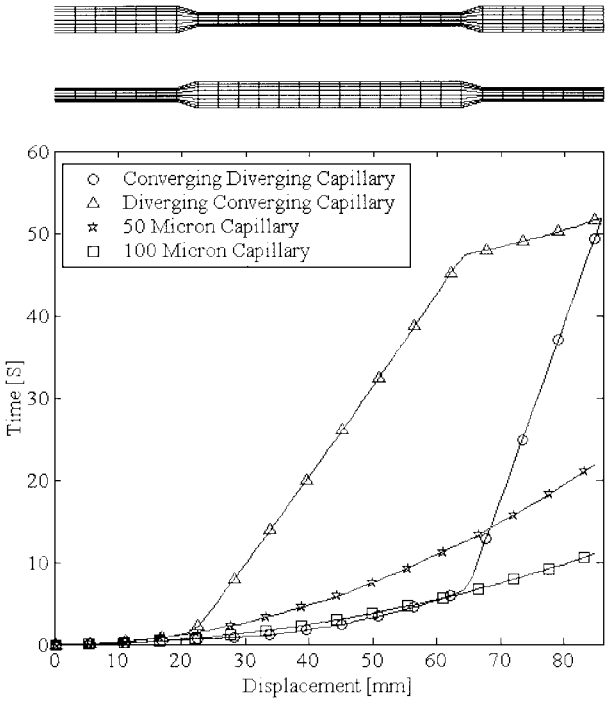

FIG. 4. Interface progression with time for converging-diverging, diverging-converging, and two straight capillaries. $D_{max} = 100$ μm, $D_{min} = 50$ μm, surface tension = 30 mN/m, $\theta_e = 30°$, and $\mu = 0.001$ kg/ms. Upper image shows irregular capillary layout.

diameter region immediately following the small diameter region (the exit region for the converging-diverging capillary and the intermediate region for the diverging-converging capillary).

This is further illustrated in Figs. 5a and 5b, which compare the interface velocity as a function of displacement for the converging-diverging capillary (5a) and the diverging-converging capillary (5b). In each case the velocity results are compared with those for a straight capillary with a diameter equivalent to that in the entrance region of the irregular capillaries. As expected over the first 20 mm, where the diameters are equivalent, the results are identical. Then, as the intermediate section is entered, a rapid increase in velocity is observed for the converging-diverging capillary and a rapid decrease in velocity is noticed for the diverging-converging capillary.

This result can be explained by examining the changes in the viscous, F_v, and capillary, F_c, forces applied to the liquid continuum as the interface passes from one region into another. For the cases considered here the viscous and the capillary forces can be approximated by the following proportionalities,

$$F_v \propto \frac{\mu V_{ave}}{D_{cap}^2}, \qquad [9a]$$

$$F_c \propto \frac{\gamma}{D_{int} L}, \qquad [9b]$$

where V_{ave} is the interface velocity, L is the distance between the atmospheric reservoir and the interface, D_{cap} is the capillary diameter upstream of the interface, and D_{int} is the capillary diameter at the interface. For straight geometries, it is apparent that for increasing capillary diameter the $1/D^2$ term in the viscous force will decrease more rapidly than the $1/D$ term in the capillary force term. The weaker viscous force (resistance force to flow) and the stronger capillary force (the driving force of the flow) act to increase the velocity, resulting in a faster interface progression. This is supported by the results shown in Fig. 4 where clearly the 100-μm-diameter capillary reaches the end of the simulation domain significantly earlier than the 50-μm capillary.

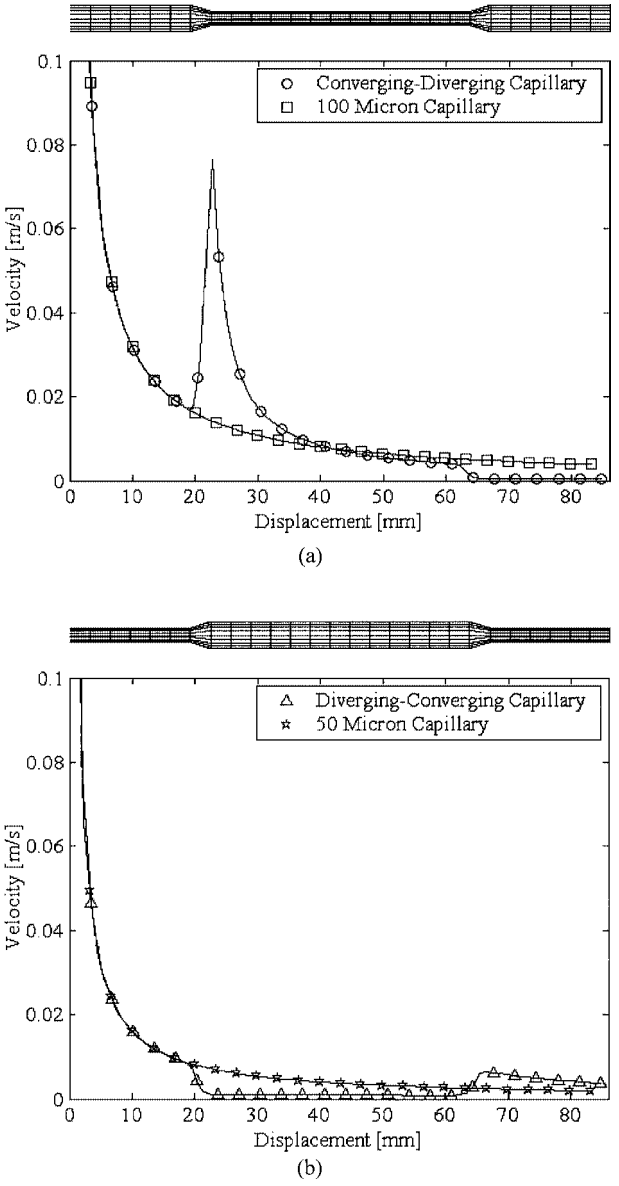

FIG. 5. Interface velocities for a (a) converging diverging capillary and a 100-μm-diameter straight capillary and a (b) diverging converging capillary and a 50-μm-diameter straight capillary. Upper image shows irregular capillary layout.

For the converging-diverging capillary, when the interface enters the intermediate zone it is apparent that the capillary force will be proportional to $1/D_{min}$, as is shown in Fig. 6. Since most of the liquid is in the entrance zone the viscous force will be dominated by the upstream diameter and thus be proportional to $1/D_{max}^2$. As a result the capillary force increases faster than the viscous force and hence the flow velocity increases, as was shown in Fig. 5a. Conversely in the diverging-converging capillary at the same location (again see Fig. 6), the capillary force is proportional to $1/D_{max}$ while the viscous force is dominated by $1/D_{min}^2$, resulting in the deceleration in the interface velocity shown in Fig. 5b. As the interface advances further downstream and enters the exit region, the opposite effect occurs where the capillary force is now proportional to $1/D_{max}$ and the viscous force is dominated by $1/D_{min}^2$ for the converging-diverging capillary resulting in a slowing of the interface velocity and vice versa for the diverging-converging capillary.

As is discussed in Section 2.1 (Eq. [7]), the dynamic contact angle is a function of the equilibrium contact angle, the system thermophysical properties, and the instantaneous interfacial speed. In the absence of a significant line tension of the three-phase contact line, the equilibrium contact angle should be independent of the capillary cross-sectional area (i.e., the radius of three-phase contact line). However, when the capillary cross-section area changes, the interfacial speed changes and hence the dynamic contact angle changes. The dynamic contact angle change will in turn affect the capillary force driving the liquid flow. This approach ignores the geometric discontinuity at the diverging-converging and converging-diverging points where the contact angle and interfacial radius suddenly change. Such points may have a localized effect on the flow; however, this is beyond the scope of this study.

In Fig. 7 the displaced volume (i.e., the wetted volume) as a function of time is shown for the same four capillaries shown in Fig. 4. As expected the displaced volume in the converging-diverging capillary is higher than that of the diverging-converging capillary over the majority of the simulation; however, the same volume is reached at the end of the computational domain. Of interest here is the fact while the average interfacial velocity of the 50-μm capillary is significantly higher than both the converging-diverging and the diverging-converging capillaries, as shown in Figs. 4 and 5, the total displaced volume tends to be significantly less than that of the converging-diverging capillary, while it is comparable to that of the diverging-converging capillary.

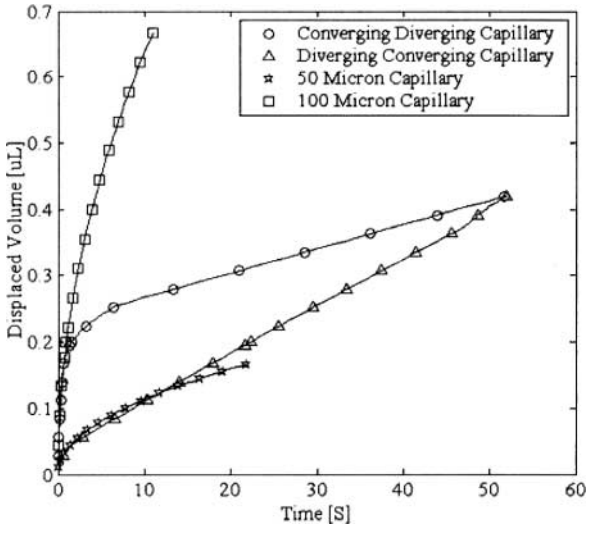

FIG. 7. Displaced volume with time for converging-diverging, diverging-converging, and two straight capillaries. $D_{max} = 100$ μm, $D_{min} = 50$ μm, surface tension = 30 mN/m, $\theta_e = 30^\circ$, and $\mu = 0.001$ kg/ms.

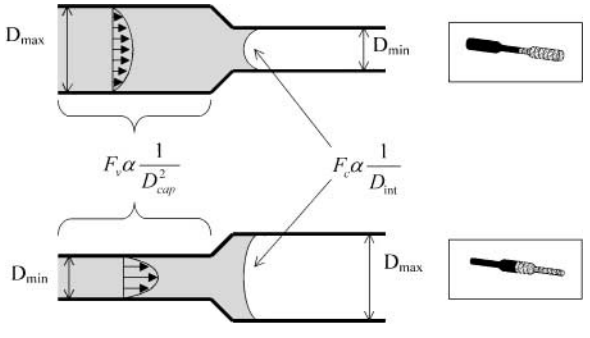

FIG. 6. Forces applied to the fluid region immediately after a change in capillary diameter. In the upper image the interface velocity will increase, since $F_c \propto 1/D_{min}$ and $F_v \propto 1/D_{max}^2$. In the lower image the interface velocity will decrease, since now $F_c \propto 1/D_{max}$ and $F_v \propto 1/D_{min}^2$.

4.2. Influence of Intermediate Zone Diameter

Figures 8a and 8b illustrate the effects of the magnitude intermediate section diameter on the interface progression with time for the converging-diverging capillary and diverging-converging capillary, respectively. With the exception of this diameter, the simulation conditions are identical to those listed above; however since the angle α was fixed at 0.5°, the regions between the entrance and intermediate zones and the intermediate and exit zones (where the diameter changes) are slightly larger for the smaller D_{min} in Fig. 8a and the larger D_{max} in Fig. 8b. In both cases as the diameter of the middle region begins to approach that of the entrance and exit regions, the average interface velocity over the simulation domain increases until it reaches a maximum when $D_{min} = D_{max}$. From this result it is apparent that in cases where the termination points are of equivalent diameter, any deviation in the cross-sectional area of the capillary will tend to decrease the overall wetting speed and therefore the fastest wetting will occur in uniform capillaries.

4.3. Multiple Irregular Regions

In the majority of cases of interest, such as wetting phenomena in porous media, multiple regions of geometric irregularity can be expected over the relatively long wetting distances discussed here. Therefore, we extend the developed model to consider

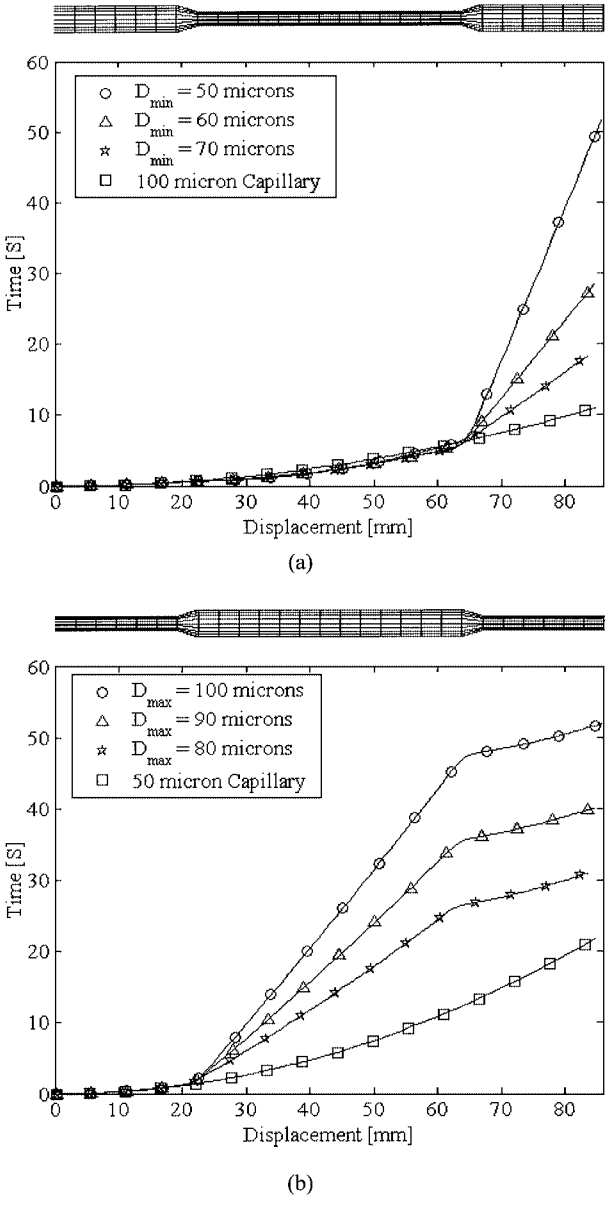

FIG. 8. (a) Effect of D_{min} on the interface progression for a converging-diverging capillary ($D_{max} = 100\ \mu$m). (b) Effect of D_{max} on the interface progression for a diverging-converging capillary ($D_{min} = 50\,\mu$m). Surface tension = 30 mN/m, $\theta_e = 30°$, and $\mu = 0.001$ kg/ms.

multiple converging-diverging and diverging-converging regions along the capillary length and compare their wetting behavior in Figs. 9a (converging-diverging case) and 9b (diverging-converging case). As in Section 4.1., the physical parameters for the simulations are $\gamma = 30$ mN/m, $\theta_e = 30°$, $\rho = 1000$ kg/m^3, $\mu = 0.001$ kg/ms, with D_{min} and D_{max} equal to 50 and 100 μm, respectively. The lengths of each individual region and the angle α were selected such that the total length of the 100-μm sections and 50-μm sections were equivalent for all cases.

In both Figs. 9a and 9b the same trends discussed in Section 4.1. can be observed for the capillaries with multiple irregularities. As expected in all cases the wetting speed increases as the interface enters a smaller diameter region from a larger diameter and decreases for the opposite case. When the two figures are compared it is also apparent that all cases reach the termination point at exactly the same time, independent of the number of irregular regions. Thus while the local wetting velocities will not be accurately predicted, a simple single converging-diverging capillary model is sufficient to predict the total wetting time independent of the total number of irregular regions, so long as a representative D_{max} and D_{min} can be obtained.

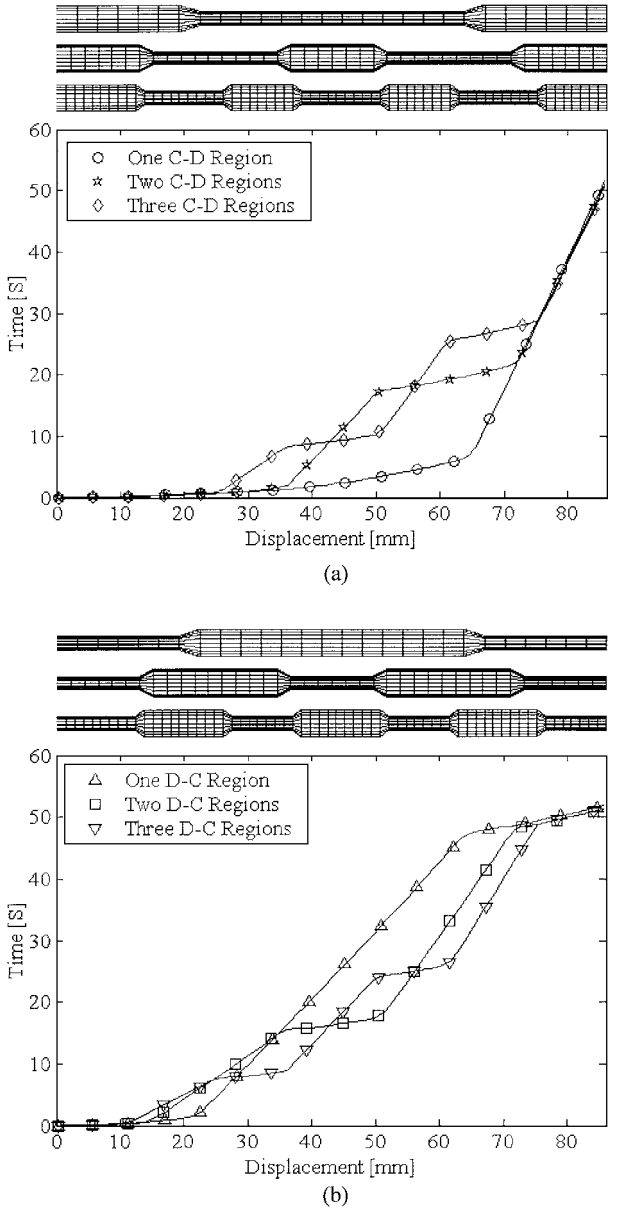

FIG. 9. Wetting behavior for capillaries with multiple (a) converging-diverging and (b) diverging-converging sections. Surface tension = 30 mN/m, $\theta_e = 30°$, and $\mu = 0.001$ kg/ms. Upper images show the irregular capillary layouts.

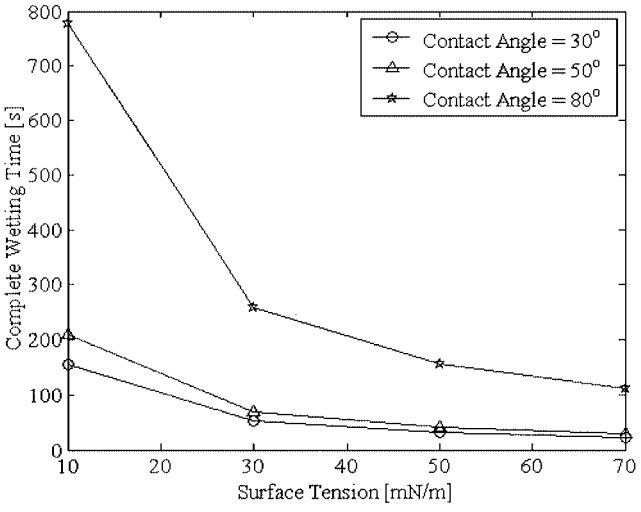

FIG. 10. Time required to completely wet a converging diverging or diverging converging capillary with $D_{max} = 100\ \mu$m, $D_{min} = 50\ \mu$m, $\alpha = 0.5^\circ$, and $\mu = 0.001$ kg/ms.

4.4. Influence of Surface Tension and Contact Angle

Figure 10 demonstrates the influence of surface tension and contact angle on the time required to completely wet a converging-diverging or diverging-converging capillary with the same geometric properties as those discussed in Section 4.1 (i.e., $D_{max} = 100\ \mu$m, $D_{min} = 50\ \mu$m, the entrance and the exit regions 20 mm long each and the intermediate section 40 mm long). As can be seen in Fig. 4, when converging-diverging and diverging-converging capillaries are compared, the total wetting time is equivalent for both geometries; thus a single figure is sufficient for both cases. As expected, Fig. 10 shows a significant increase in the total wetting time with decreasing surface tension, requiring approximately 13 min at 10 mN/m vs just over 2 min at 70 mN/m for the high contact angle case.

Table 1 compares the total wetting time, t_{wet}, of a converging-diverging capillary with that of a straight capillary for various surface tension, γ, and equilibrium contact angle, θ_e, values. In each case, t_{wet} has been scaled by the result for equivalent contact angle and geometry, but a surface tension of 10 mN/m. As can be seen in each case, the scaled results are identical, suggesting that, for the cases examined here, the degree to which the magnitude of the surface tension and contact angle affect the fill time is independent of the capillary geometry.

TABLE 1

Time Required to Completely Wet a Straight Capillary and a Converging-Diverging Capillary, for Different Surface Tension and Equilibrium Contact Angle Values

	$t_{wet}(\gamma = 70$ mN/m)/ $t_{wet}(\gamma = 10$ mN/m)	$t_{wet}(\gamma = 30$ mN/m)/ $t_{wet}(\gamma = 10$ mN/m)
C–D capillary ($\theta_e = 30^\circ$)	0.14	0.33
Straight capillary ($\theta_e = 30^\circ$)	0.14	0.33
C–D capillary ($\theta_e = 80^\circ$)	0.14	0.33
Straight capillary ($\theta_e = 80^\circ$)	0.14	0.33

5. CONCLUSIONS

In this study the surface tension-driven, dynamic wetting of converging-diverging and diverging-converging capillary tubes was investigated through finite-element-based numerical simulations. A simple interface tracking and reconstruction procedure has been described. This procedure tracks changes in the total liquid volume in the capillary to determine the interface location and uses Cox's formulation to determine the dynamic contact angle. The numerical code and interface tracking procedure are verified by examining the rising of a liquid in a vertical capillary and comparing the results with the well-known Lucas-Washburn Equation.

In general it was found that the surface tension-driven flow was significantly slower in both converging-diverging and diverging-converging capillaries than in straight capillaries with comparable diameters. The difference was attributed to the slow interface advancement when the liquid enters a larger diameter region from a smaller diameter region, where the capillary force is at a minimum and the viscous force is at a maximum. By comparing different values for the diameter of the middle section of the capillary, it was determined that for capillaries with equivalent inlet and outlet diameters the fastest wetting will always occur in straight capillaries and any deviation in the capillary diameter along its length will slow the wetting speed. In addition, it was found that while the local wetting speeds differ significantly the total wetting time is independent of the number of irregular regions along the capillary length, suggesting that a simple converging-diverging model is sufficient for predicting this quantity. The effects of contact angle and surface tension on the total wetting time of the converging-diverging and diverging-converging capillaries were found to be similar to those for straight capillaries.

APPENDIX A: COMPUTATIONAL PROCEDURE

As detailed in Section 2.1, in this study a simple volume displacement approach combined with Cox's formulation has been used to track the interface location and shape with time. Detailed below is the computational procedure used to implement this approach.

1. At the beginning of each time step an initial dynamic contact angle is assumed based on the value at the previous time step and an initial computational mesh is formed.

2. The flow field is determined by solving Eqs. [1] and [2] subject to the stress conditions at the interface defined by Eqs. [4] over the current mesh.

3. From the current flow field, the volume flux into the computational domain is calculated and multiplied by the time step, Δt, to determine the volume of liquid entering the system. This

value is then used to determine the interface location at the end of the time step.

4. Based on this estimated displacement the capillary number is calculated and then used to calculate the dynamic contact angle based on Cox's formulation.

5. If the dynamic contact angle calculated in 4 is the same as that used in 2, with some specified tolerance, the interface location is updated and steps 1 through 5 are repeated until the simulation is complete. Otherwise the computational domain is remeshed based on the updated value of the dynamic contact angle and steps 2 through 4 are repeated until convergence on the contact angle is obtained.

APPENDIX B: NOMENCLATURE

Ca	capillary number, $Ca = \mu v_o/\gamma$
D	capillary diameter [m]
D_{cap}, D_{int}	capillary and interface diameters [m]
D_{min}, D_{max}	minimum and maximum capillary diameters [m]
F_r, F_z	nondimensional general body forces in the r and z coordinate directions
F_v, F_c	viscous and capillary body forces
Q	volume flow rate [m^3/s]
R, Z	nondimensional coordinate directions ($R = r/r_o$, $Z = Z/r_o$)
R_1, R_2	nondimensional radii of curvature at the interface
V_r	nondimensional velocity in the r direction ($V_r = v_r/v_o$)
V_z	nondimensional velocity in the z direction ($V_z = v_z/v_o$)
g	gravitational constant [m/s^2]
h	height of the capillary rise [m]
s	characteristic dimension of the flow system ($s = r_o$)
r, z	coordinate directions [m]
t	time [s]
v_o	reference velocity [m/s]
v_r	r component of velocity [m/s]
v_z	z component of velocity [m/s]

Greek Symbols

Δt	time step [s]
Γ	vector describing the location of a point on the surface
Ω	computational domain
α	convergent/divergent angle of capillary [degrees]
ε_s	microscopic slip length [m]
γ	surface tension [N/m]
λ	ratio of viscosities, μ_{air}/μ_{fluid}
μ	viscosity [kg/ms]
θ_e, θ_d	equilibrium and dynamic contact angle [degrees]
τ_{nt}, τ_{nn}	nondimensional normal and tangential components of the stress tensor
τ_{rr}, τ_{rz}, τ_{zz}	nondimensional components of the Cartesian stress tensor

ACKNOWLEDGMENTS

The authors thank the financial support of the Natural Sciences and Engineering Research Council through a scholarship to David Erickson and through a research grant to D. Li and C. B. Park.

REFERENCES

1. Lucas, R., *Kolloid Z.* **23,** 15 (1918).
2. Washburn, E. W., *Phys. Rev.* **17,** 273 (1921).
3. Rideal, E. K., *Philos. Mag. Ser.* **44,** 1152 (1922).
4. Bosanquet, C. H., *Philos. Mag. Ser.* **45,** 525 (1923).
5. Quéré, D., Raphael, E., and Ollitrault, J.-Y., *Langmuir* **10,** 3679 (1999).
6. Zhmud, B. V., Tiberg, F., and Hallstensson, K., *J. Colloid Interface Sci.* **228,** 263 (2000).
7. Tay, A. O. O., Huang, Z. M., and Wu, J. H., IEEE/CPMT Electronic Packaging Technol. Conf., 263 (1997).
8. Han, S., Wang, K. K., and Cho, S.-Y., *IEEE Electronic Components and Technol. Conf.*, 327 (1996).
9. Schwiebert, M. K., and Leong, W. H., *IEEE Trans. Components Packaging Manuf. Technol.* **19,** 133 (1996).
10. Chippada, S., Jue, T. C., and Ramaswamy, B., *Int. J. Numerical Methods Eng.* **38,** 335 (1995).
11. Housiadas, K., Georgiou, G., and Tsamopoulos, J., *Int. J. Numerical Methods Fluids* **33,** 1099 (2000).
12. Mason, G., and Morrow, N. R., *J. Colloid Interface Sci.* **141,** 262 (1991).
13. Turian, R., and Kessler, F., *AIChE J.* **46,** 695 (2000).
14. Mason, G., and Morrow, N. R., *J. Colloid Interface Sci.* **168,** 130 (1994).
15. Lin, C.-Y., and Slattery, J. C., *AIChE J.* **28**(2), 311 (1982).
16. Lowdes, J., *J. Fluid Mech.* **101,** 631 (1980).
17. Bazhlekov, I. B., and Chesters, A. K., *J. Fluid Mech.* **329,** 137 (1996).
18. Tilton, J. N., *Chem. Eng. Sci.* **43,** 1371 (1988).
19. Welsh, J. E., Harlow, F. H., Shannon, J. P., and Daly, B. J., Los Alamos Scientific Laboratory Report LA-3425, 1966.
20. Cox, R. G., *J. Fluid Mech.* **168,** 169 (1986).
21. Basu, S., Nandakumar, K., and Masliyah, J. H., *J. Colloid Interface Sci.* **190,** 253 (1997).
22. Gu, Y., and Li, D., *Colloids Surf. A* **142,** 243 (1998).
23. Basu, S., Nandakumar, K., and Masliyah, J. H., *J. Colloid Interface Sci.* **182,** 82 (1996).
24. Heinrich, J. C., and Pepper, D. W., "Intermediate Finite Element Method," Taylor & Francis, Philadelphia, 1999.